

MeV-scale performance of water-based and slow liquid scintillators

B. J. Land,^{1,2,3} Z. Bagdasarian,^{2,3} J. Caravaca,^{2,3} M. Smiley,^{2,3} and G. D. Orebi Gann^{2,3}

¹*University of Pennsylvania, Philadelphia, PA, USA*

²*University of California, Berkeley, CA 94720-7300, USA*

³*Lawrence Berkeley National Laboratory, CA 94720-8153, USA*

This paper presents studies of the performance of water-based liquid scintillator in both 1-kt and 50-kt detectors. Performance is evaluated in comparison to both pure water Cherenkov detectors and a nominal model for pure scintillator detectors. Performance metrics include energy, vertex, and angular resolution, along with a metric for ability to separate the Cherenkov from the scintillation signal, as being representative of various particle identification capabilities that depend on the Cherenkov / scintillation ratio. We also modify the time profile of scintillation light, including both the rise and decay times, to study the same performance metrics in slow scintillators. We go on to interpret these results in terms of their impact on certain physics goals, such as solar neutrinos and the search for Majorana neutrinos. We show that a 50-kt detector would be capable of better than 10 (1)% precision on the CNO neutrino flux with a WbLS (pure LS) target, as well as sensitivity into the normal hierarchy region for Majorana neutrinos, with half life sensitivity of $T_{1/2}^{0\nu\beta\beta} > 1.4 \times 10^{28}$ years at 90% CL for 10 years of data taking with a Te-loaded target.

I. INTRODUCTION

These are exciting times for neutrino physics, with a number of open questions that can be addressed by next-generation detectors. Advances in technology and innovative approaches to detector design can drive the scientific reach of these experiments. A hybrid optical neutrino detector, capable of leveraging both Cherenkov and scintillation signals, offers many potential benefits. The high photon yield of scintillators offers good resolution and low thresholds, while a clean Cherenkov signal offers ring imaging at high energy, and direction resolution at low energy. The ratio of the two components provides an additional handle for particle identification that can be used to discriminate background events.

One approach to achieving a hybrid detector is to deploy water-based liquid scintillator (WbLS) [1], a novel target medium that combines water with pure organic scintillator, thus leveraging the benefits of both scintillation and Cherenkov signals in a single detection medium, with the advantage of high optical transparency and, thus, good light collection. There is significant effort in the community to develop this technology, including target material development [1–12], demonstrations of Cherenkov light detection from scintillating media [13–16], demonstrations of spectral sorting [17, 18], fast and high precision photon detector development [19–26], complementary development of reconstruction methods and particle identification techniques [27–33], and development of a practical purification system at UC Davis.

Many experiments are pursuing this technology for a range of applications, including a potential ton-scale deployment at ANNIIE at FNAL [34–36], possible kt-scale deployments at the Advanced Instrumentation Testbed (AIT) facility in the UK [37–39] and in Korea [40], and, ultimately, a large (25–100 kt) detector at the Long Baseline Neutrino Facility, called THEIA. The THEIA program builds heavily on early developments by the LENA col-

laboration [41]. Such a detector could achieve an incredibly broad program of neutrino and rare event physics, including highly competitive sensitivity to long-baseline neutrino studies, astrophysical searches, and even scope to reach into the normal hierarchy regime for neutrinoless double beta decay [42–45].

In this paper, we study the low-energy performance of such a detector for a range of different target materials, and compare the results to that for a pure water Cherenkov detector, and a pure liquid scintillator detector, using linear alkyl benzene (LAB) with 2 g/L of the fluor 2,5-Diphenyloxazole (PPO) as the baseline for comparison. Properties for the pure LS detector are taken from measurements by the SNO+ collaboration [46, 47]. We start by considering three WbLS target materials, based on bench-top measurements of properties reported in [14, 48]. Each cocktail is a combination of water with LAB+PPO, with differing fractions of the organic component: 1, 5 and 10% concentration by mass. The light yield for each material is taken from [14], with the time profile and emission spectrum taken from [48]. Other properties are evaluated based on the composition of the material, as described in Sec. II. Measurements of these particular WbLS materials demonstrated a very fast timing response: with a rise time consistent with 0.1 ns, and a prompt decay time on the order of 2.5 ns. These measurements were confirmed with both x-ray excitation [48] and direct measurements with β and γ sources [14]. Since this fast time profile increases the overlap between the prompt Cherenkov and delayed scintillation signals, we also consider materials in which we delay the scintillation time profile by some defined amount, to study the impact of a “slow scintillator”, for both pure LS and WbLS. Such materials are under active development [4, 5].

Metrics used for these performance studies include the energy resolution (dominated by photon counting and quenching effects), vertex resolution, direction resolution, and a statistic chosen to represent the separability of the Cherenkov and scintillation signals. This is repre-

representative of low-energy performance capabilities such as particle identification, which may rely on separating the two populations. The final choice of a detector material for any particular detector would depend on the physics goals, which will place different requirements on each aspect of detector performance. In all cases, we focus on the low-energy regime. Performance studies at the high energies relevant for neutrino beam physics are underway, and will depend on a different combination of factors, so may yield different optimizations.

We consider both a kt-scale and a 50-kt scale detector, as being representative of experiments currently under consideration. We consider four options for photodetectors: a “standard” photomultiplier tube (PMT), with a transit time spread (TTS) of 1.6 ns, fast PMTs with a 1 ns TTS, faster PMTs with a 500 ps TTS, and very fast photon detectors, such as large-area picosecond photon detectors (LAPPDs) [49], with a TTS of 70 ps. In each case we assume 90% coverage, with a representative quantum efficiency (QE) used for all four models.

To understand the impact of the detector capabilities studied here, we discuss the impact for several low-energy physics goals, in particular considering scope for a precision measurement of CNO solar neutrinos, and normal hierarchy sensitivity for neutrinoless double beta decay (NLDBD) [42, 45]. Large-scale scintillator detectors such as Borexino [50] and KamLAND-Zen [51] are leaders in the fields of solar neutrinos and searches for NLDBD, respectively, and new scintillator detectors such as SNO+ [46] and JUNO [52, 53] are taking data or under construction. There is much interest in the community in using new solar neutrino data for precision understanding of neutrino properties and behavior, as well as for solar physics [54]. The proposed THEIA experiment has discussed and evaluated the potential of a multi-kiloton, high-coverage WbLS detector for the purposes of solar neutrino detection and NLDBD [42, 44], where the latter would deploy inner containment for an isotope-loaded pure LS target, adapting techniques from SNO+ and KamLAND-Zen. Studies such as those presented here can help to inform future detector design.

Sec. II presents details of the scintillator model used. Sec. III describes the simulation and analysis methods, including the reconstruction algorithms applied. Sec. IV presents results for performance of the measured WbLS cocktails, including photon counting and reconstruction capabilities. Sec. V presents the results for slow scintillators, considering both the pure LS and a 10% WbLS. Sec. VI discusses these performance results in light of their impact on certain selected physics goals, and Sec. VII concludes.

II. WATER-BASED LIQUID SCINTILLATOR MODEL

For Monte Carlo simulation of photon creation and propagation in WbLS, we use the Geant4-based [55]

RAT-PAC framework [56]. Cherenkov photon production is handled by the default Geant4 model, G4Cherenkov. Rayleigh scattering process is implemented by the module developed by the SNO+ collaboration [47]. The GLG4Scint model handles the generation of scintillation light, as well as photon absorption and reemission. We utilize the light yield as measured in WbLS (1%, 5%, and 10% solutions) in Ref. [14], and scintillation emission spectrum and time profile as taken from Ref. [48]. Other inputs to the water-based liquid scintillator optical model have not yet been measured directly, and, hence, are estimated from those of water and LAB+PPO, as described below.

A. Refractive index estimation

In order to estimate the refractive index for WbLS, n , we use Newton’s formula for the refractive index of liquid mixtures [57]:

$$n = \sqrt{\phi_{labppo} n_{labppo}^2 + \phi_{water} n_{water}^2}, \quad (1)$$

where ϕ denotes the volume fraction of a corresponding component, while n_{labppo} and n_{water} correspond to the measured refractive indexes for LAB+PPO [47] and water [58]. Due to the dominant fraction of water, the WbLS refractive index is very similar to that of pure water.

B. Absorption and scintillation reemission

The absorption coefficient, α , of WbLS depends on the molar concentration, c , of each of the components as:

$$\alpha(\omega) = c_{lab} \epsilon_{lab}(\omega) + c_{ppo} \epsilon_{ppo}(\omega) + c_{water} \epsilon_{water}(\omega), \quad (2)$$

where ϵ_{lab} , ϵ_{ppo} and ϵ_{water} are the molar absorption coefficients of LAB, PPO [47], and water (taken from Ref. [59] for wavelengths over 380 nm and from Ref. [60] for wavelengths below 380 nm).

A photon absorbed by the scintillator volume has a non-zero probability of being reemitted. This reemission process becomes important at low wavelengths where the absorption by scintillator is dominant. As a result, photons are shifted to longer wavelengths where the detection probability is higher due to a smaller photon absorption and a greater PMT quantum efficiency. The probability p_i^{reem} of a component i absorbing a photon of frequency ω is determined as the contribution of the given component to the total WbLS absorption coefficient:

$$p_i^{reem}(\omega) = \phi_i \alpha_i(\omega) / \alpha(\omega), \quad (3)$$

where ϕ_i is the volume fraction of component i in WbLS. After a photon is absorbed, it can be reemitted with a 59% probability for LAB and an 80% probability for PPO [47], following the primary emission spectrum.

C. Scattering length

The Rayleigh scattering length, λ^s , is estimated for WbLS as:

$$\lambda^s(\omega) = (\phi_{lab}\lambda_{lab}^{-1}(\omega) + \phi_{water}\lambda_{water}^{-1}(\omega))^{-1}, \quad (4)$$

where λ_{lab} and λ_{water} are the scattering lengths for LAB and water, respectively, both taken from [47]. It was noted that the addition of PPO does not change λ^s and thus it is omitted in Eq. 4.

The resulting values of both absorption and scattering lengths for WbLS are close to those of pure water. It is possible that this method overestimates the attenuation lengths, in particular, the scattering, given the complex chemical structure and composition of WbLS. A long-arm measurement of WbLS absorption and scattering lengths is planned in the near future.

III. SIMULATION AND ANALYSIS METHODS

The WbLS models developed in [61], and described above, can be used to evaluate the performance of these materials in various simulated configurations. Of interest are large, next-generation detectors such as THEIA [42], which could contain tens of kilotons of target material instrumented with high quantum efficiency photodetectors at high coverage, and proposed detectors in the range of one to a few kt, such as AIT [37]. To evaluate these materials, two detector configurations are simulated: a 1-kt detector and a 50-kt detector, both with 90% coverage of photon detectors as a baseline. The different concentration WbLS materials studied in [14], 1%, 5% and 10% WbLS, are simulated and compared to both water and pure (100%) scintillator material LAB+PPO [47].

A. Monte Carlo simulation

Fully simulating next-generation detector sizes instrumented with 3D models of photon detectors at the desired coverage of 90% requires significant computational resources. This is especially true when studying multiple geometries, as the simulation typically must be rerun for each geometry. To avoid this redundancy, RAT-PAC [56] can easily simulate a sufficiently large volume of material and export the photon tracks to an offline geometry and photon detection simulation. Using this method, 2.6-MeV electrons are simulated at the center of a large volume of target material, isotropic in direction, and the resulting tracks are stored for later processing by a detector geometry model and a photon detector model. This energy is chosen as being representative of a number of low-energy events of interest, including reactor antineutrinos, low-energy solar neutrinos, and the end-point of double beta decay for both ^{136}Xe and ^{130}Te .

1. Detector geometry

Each detector configuration is modeled as a right cylinder with diameter and height of 10.4 m and 38 m for the 1-kt and 50-kt sizes, respectively. Specifically, this calculation achieves a 1-kt and 50-kt total mass for the LAB+PPO detector, with slightly modified target masses for the other target materials, based on different densities. The photon tracks from stored events that are found to intersect with the cylinder representing the detector boundary are stored as potential detected photons (“hits”) for each event. In this way, the boundary of each active volume acts as a photon-detecting surface that provides all information about each photon to a photon detector model.

2. Photon detection

Photon detectors vary in their probability of detecting a photon as a function of wavelength (the QE) and their time resolution (TTS). Four photon detector models are considered for each material and geometry:

1. “*PMT*” a modern large-area high-QE PMT such as an R5912-100 [62] with 34% peak QE and 1.6-ns TTS.
2. “*FastPMT*” a hypothetical PMT with a similar QE but smaller TTS of 1.0 ns.
3. “*FasterPMT*” a hypothetical PMT again with a similar QE but even smaller TTS of 500 ps.
4. “*LAPPD*” a next-generation device such as a large-area picosecond photodetector (LAPPD) [49] with similar QE but a 70-ps TTS.

The same QE is used for all four models, assuming that future LAPPDs can reach comparable QE to existing Hamamatsu large-area PMTs.

A coverage of 90% using these devices is simulated by accepting only 90% of potential hits for the event. The QE is accounted for by randomly accepting hits according to the value of the QE curve (shown in Fig. 1 with typical wavelength spectra) at the wavelength of the hit. For the selected hits, the intersection position with the geometry model is taken as the detected position. Finally, a normally distributed random number with a width corresponding to the TTS of the photon detector model is added to the truth time of the hit to get the detected time. These detected hit position and times can then be passed to reconstruction algorithms for further analysis.

B. Event reconstruction

To evaluate the performance of the different materials under different detector configurations, a fitter was developed to reconstruct the initial vertex parameters based

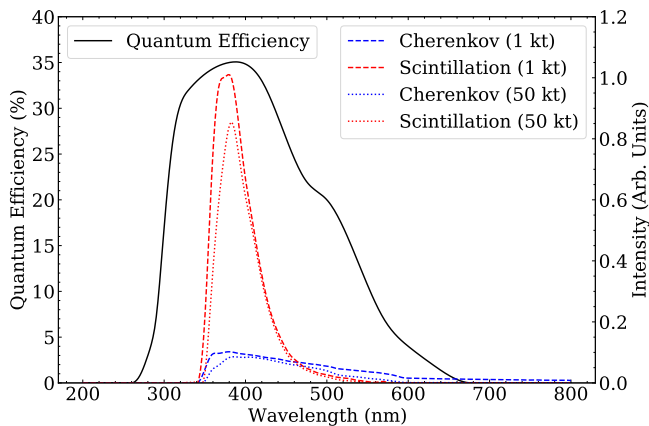


FIG. 1. The quantum efficiency (QE) used for photon detector models considered here (digitized from [62]). Also shown are Cherenkov and scintillation spectra for the 1% WbLS material in the two detector sizes prior to application of QE. The relative normalization of the spectra have been preserved, with the maximum value normalized to 1.0.

on detected hit information. Position and time reconstruction are both aided by the large number of isotropic scintillation photons, while direction reconstruction relies on identification of non-isotropic Cherenkov photons. As Cherenkov photons are prompt with respect to scintillation photons, the reconstruction will first identify prompt photons, and then use them to reconstruct direction in a staged approach. Promptness is defined in terms of the hit time residual t_{resid} distribution.

The reconstruction algorithm used here has the following steps, which are described in detail in the following sections:

- Step 1: Position and time are reconstructed using all detected hits.
- Step 2: Reconstructed position and time are used to compute the t_{resid} distribution for detected hits.
- Step 3: Direction is reconstructed using only hits before some t_{cut} on the t_{resid} distribution with position and time fixed.
- Step 4: Finally, the total number of hits is recorded as an estimate of the energy of the event.

The approach is inspired by vertex reconstruction algorithms used in the SNO experiment [63]. The algorithm has been tested and demonstrated to achieve similar position and direction resolution to SNO for equivalent event types in a SNO-like detector—for example, for 5 MeV electrons in a SNO-sized vessel, with TTS and photo-coverage set to relevant values (approximately 1.8 ns and 55%, respectively) this algorithm achieves 27.4° angular resolution, compared to the SNO reported value of 27°.

1. Position and time

Reconstructing vertex position and time can be done by maximizing the likelihood of $t_{resid,i}$ for each hit i in the event:

$$t_{resid,i} = (t_i - t) - |\vec{x}_i - \vec{x}| \frac{c}{n}, \quad (5)$$

where (\vec{x}_i, t_i) are the position and time of a detected photon, (\vec{x}, t) represents the fitted vertex position and time, and $\frac{c}{n}$ is the group velocity typical of a 400-nm photon. This expression includes two important assumptions that are made to approximate a realistic detection scheme.

1. The travel time is calculated assuming a photon wavelength of 400 nm, since for a real detector the wavelength is typically not known. Fig. 1 shows the expected spectra for both Cherenkov and scintillation light.
2. Each photon is assumed to travel in a straight line, as photon detectors are typically not aware of the actual path the photon traveled.

A result of these assumptions is that dispersion in the material will broaden the t_{resid} distribution, as the travel time will be overestimated (underestimated) for longer (shorter) wavelength photons. Additionally, scattered or reemitted photons will appear later than their true emission time due to ignoring their true path. An example of a t_{resid} distribution using the true detection times, but with these approximations, is shown for the 10% WbLS and LAB+PPO material in Fig. 2 for the 1-kt and 50-kt detector geometries. In plots shown in this paper, the t_{resid} is arbitrarily shifted such that the average t_{resid} of Cherenkov photons across many events is 0 ns. The integral of these distributions is the number of detected photons per event on average, which highlights both the difficulty of identifying Cherenkov photons in pure scintillators, and their prompt placement in the t_{resid} distribution.

For each material and detector configuration, a PDF for t_{resid} of all photons is produced using truth information from a subset of the simulated events. Reconstruction is then done by minimizing the sum of the negative logarithm of the likelihood for each hit with a two-staged approach: a Nelder-Mead [64] minimization algorithm with a randomly generated seed is used to explore the likelihood space and approximate the global minima, followed by a BFGS [64] minimization algorithm to find the true (local) minima using the minima from the previous step as the seed. This method produces the best estimate of the true t_{resid} distribution for each event, to be used in the direction fit. Residual distributions are calculated for position and time, and fit to Gaussian distributions. Position residuals are fit in a reference frame where the z axis is aligned with the true event direction. The position resolutions reported here are the quadrature sum of the widths in all three dimensions.

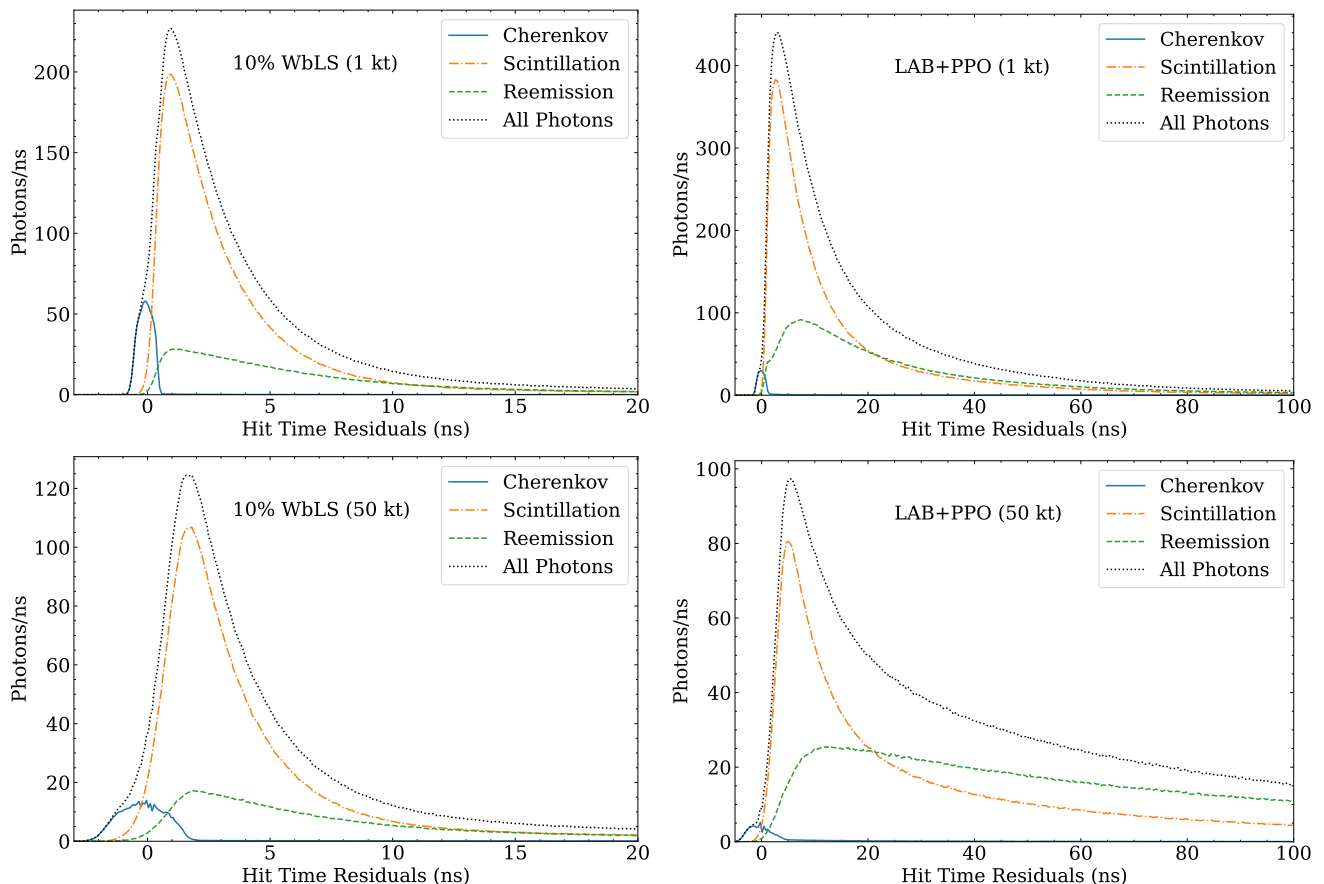


FIG. 2. True hit time residual distributions for (top left) 10% WbLS in 1-kt detector, (top right) LAB+PPO in 1-kt, (bottom left) 10% WbLS in 50-kt detector, and (bottom right) LAB+PPO in 50-kt detector. This uses the same QE as the photon detector models, but with zero TTS.

2. Direction

As Cherenkov light has a conical/ring geometry, Cherenkov hits can be used to infer the event direction. A method for doing this is by maximizing the likelihood of the cosine of the angle, θ_i , between the vector from the reconstructed event position, \vec{x} , to each detected photon position, \vec{x}_i , and a hypothesized direction \hat{d} :

$$\cos \theta_i = \frac{(\vec{x}_i - \vec{x}) \cdot \hat{d}}{|\vec{x}_i - \vec{x}|}. \quad (6)$$

For Cherenkov light, the PDF for this distribution is peaked at the Cherenkov emission angle, θ_c , of the material. Because non-Cherenkov photons do not carry directional information, they will appear flat in this distribution, and will degrade the performance of the fit. It is beneficial, therefore, to restrict this likelihood maximization to only photons with $t_{resid} < t_{cut}$ for some t_{cut} , as this should maximize the number of Cherenkov photons relative to other photons. Here, the impact of dispersion is typically beneficial, as the broad spectrum of Cherenkov light compared to typical scintillation spectra results in long-wavelength Cherenkov photons appearing

earlier in the t_{resid} distribution compared to their true emission times. We note that a photon detection scheme that can distinguish between long and short wavelength photons [18] could further enhance the ability to identify Cherenkov photons.

PDFs for the $\cos \theta_i$ distribution are created using subsets of the simulated events for many t_{cut} values between -1 ns and 10 ns, and event reconstruction is done for each t_{cut} value for every event. Reconstruction proceeds in the same way as the position-time minimizing the sum of the negative logarithms of the likelihood of each selected hit with a randomly seeded coarse Nelder-Mead [64] search, followed by a BFGS [64] method seeded with the result of Nelder-Mead to find the best minima. The value $\cos \theta$ is calculated for each reconstructed direction as $\hat{d} \cdot \hat{d}_{true}$, where \hat{d}_{true} is the initial direction of the electron. The $\cos \theta$ distribution from each simulated configuration and t_{cut} pair is integrated from $\cos \theta = 1$ until the $\cos \theta$ value that contains 68% of events, and this value is defined as the angular resolution for that pair. Finally, the angular resolution resulting from the t_{cut} with the best angular resolution for each configuration is taken as the angular resolution for that configuration.

3. Energy

The distribution of the total number of hits is fit to a Gaussian to determine the mean μ_N and standard deviation σ_N of detected hits for each condition. The fractional energy resolution is reported as σ_N/μ_N .

IV. PERFORMANCE OF WATER-BASED LIQUID SCINTILLATOR IN A LARGE-SCALE NEUTRINO DETECTOR

The materials described in Sec. III were simulated in the two detector geometries (1 kt and 50 kt) and four photodetector models (“PMT,” “FastPMT,” “FasterPMT,” and “LAPPD”) described in the same section. Between 10,000 and 100,000 events were simulated for each material, with fewer events for the pure LS due to the high photon counts (and accordingly slower simulation times). The following sections explore the true MC information provided by those simulations, as well as presenting the reconstruction results for all cases.

A. Photon population statistics

Roughly speaking, energy resolution is limited by the total number of detected photons, position and time resolution are limited by the number of direct photons (not absorbed and reemitted, scattered, or reflected), and direction resolution is limited by the number of Cherenkov photons and how visible they are within the brighter scintillation signal. The total population of photons can be broken down into the following categories:

1. *Cherenkov* photons, which were not absorbed and reemitted by the scintillator.
2. *Scintillation* photons, which were not absorbed and reemitted by the scintillator.
3. *Reemitted* photons, regardless of their origin.

These populations are shown in Fig. 3 for the materials and detector sizes considered here. Since each considered photon detector model has the same QE and coverage, the populations are the same in each case.

Higher scintillator fractions are very advantageous from an energy resolution perspective, having many more total photons. The same is true from the perspective of position and time resolution in a 1-kt detector. For a larger 50-kt detector, the population of reemitted photons for LAB+PPO is greater than the scintillation population, hinting that attenuation and reemission in pure scintillators may be disadvantageous in larger detectors. Interestingly, simulations indicate that there are more Cherenkov photons detected in LAB+PPO than in the other materials, though fraction of detected hits that are Cherenkov is much smaller. The larger refractive index of

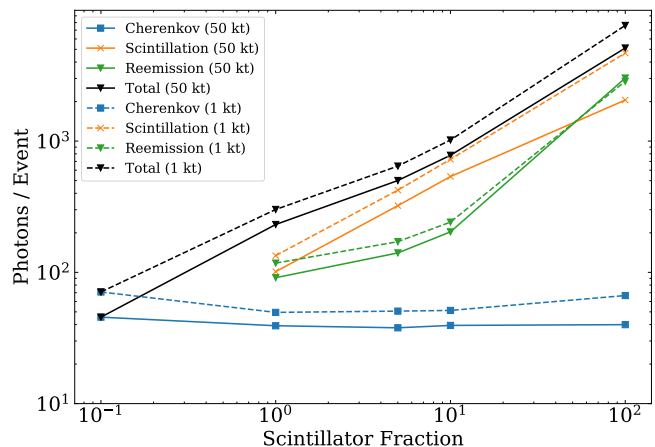


FIG. 3. The number of detected photons for 2.6-MeV electrons simulated at the center of two detector geometries (50-kt and 1-kt) differing in size. These photon counts are shown as a function of material scintillator fraction. Water is artificially plotted at 10^{-1} (due to log scale).

LAB+PPO results in more primary Cherenkov photons compared to water, and this competes with the greater absorption in pure scintillators. The lower scintillator fractions have refractive indexes closer to that of water, and the additional absorption compared to water results in fewer Cherenkov photons detected.

B. In-ring photon counting

Without applying reconstruction algorithms, one can inspect the truth information for the detected hits to understand their origins and time distributions. Of interest here is how discernible the Cherenkov photons are, and how well they may be identified against a scintillation background. Since Cherenkov photons are emitted at a particular angle θ_c with respect to the track of the charged particle, it is instructive to see how many hits are detected in the region $\theta_c \pm \delta$ (“in-ring”) with respect to the event direction. Further, since Cherenkov photons are prompt with respect to scintillation photons, it is instructive to see these populations as a function of how early they arrive. As in the reconstruction algorithm, this is defined in terms of the hit time residual, t_{resid} , where smaller t_{resid} values are more prompt.

Fig. 4 shows the number of Cherenkov and other (scintillation and re-emitted) photons for photons with $\cos \theta$ satisfying $\theta_c \pm 15^\circ$ using true detected times (TTS = 0) and true origins, but including the effect of photodetector coverage and QE, as a function of a promptness cut on t_{resid} . Of particular note is that there are more “in-ring” Cherenkov photons than other photons for sufficiently prompt t_{resid} cuts for all materials using truth information.

With the number of in-ring Cherenkov photons defined as S and the number of in-ring other-photons defined as

B , a single metric, $S/\sqrt{(S+B)}$, for the significance of the Cherenkov photons as a function of a prompt cut on t_{resid} is shown in Fig. 5. The larger this significance, the easier it should be to identify the Cherenkov topology on top of the isotropic scintillation background. The high significance at early times in the LAB+PPO material can be understood as a combination of dispersive effects, differences in scintillation time profile, and the higher refractive index in this material relative to the WbLS materials in general. Dispersion separates the narrow scintillation spectrum from the longer-wavelength tail of the Cherenkov photons in large detectors, pushing the longer-wavelength Cherenkov hits earlier, while a higher refractive index results in more Cherenkov production. The LAB+PPO material has both a larger refractive index and more dispersion than the other materials. Additionally, the measurements from [14] show the time profile of WbLS materials is faster than LAB+PPO, bringing scintillation light earlier in those materials. However, the greatest significance of Cherenkov detection in scintillating materials is achieved in WbLS, for slightly later cuts on t_{resid} .

C. Reconstruction results

Inspecting the truth information provides a detailed understanding of the information available, however, to truly evaluate these materials, it is necessary to apply reconstruction algorithms and evaluate the impact on position, time, and direction reconstruction. This is done using the reconstruction algorithm described in Sec. III and the results are shown in Fig. 6. An example view of the fit residuals for LAB+PPO with a 1.0 ns prompt cut, showing the Gaussian fits to those residuals, can be found in Fig. 7. These results are a function both of material properties and the reconstruction algorithm used, and therefore should not be taken as the best possible resolutions achievable when using these materials.

In general, the scintillator materials outperformed water in the metric of position and time resolution due to the much larger number of photons detected from scintillation light. The 1-kt detector typically demonstrates smaller residuals in position and time compared to the 50-kt detector, as the impact of dispersion and scattering, which broaden the t_{resid} distribution, are greater in the larger geometry. In particular, the better transparency of WbLS compared to LAB+PPO is evident in the relatively poorer position resolution seen with LAB+PPO when compared to 10% WbLS in the 50-kt detector. Position and time resolutions unsurprisingly improve with the reduction in TTS from the PMT model to the LAPPD model.

For direction reconstruction, the water material acts as an excellent baseline with best resolution, having only Cherenkov hits and excellent transparency. The additional scintillation light from the WbLS materials degrades this resolution by approximately a factor of two

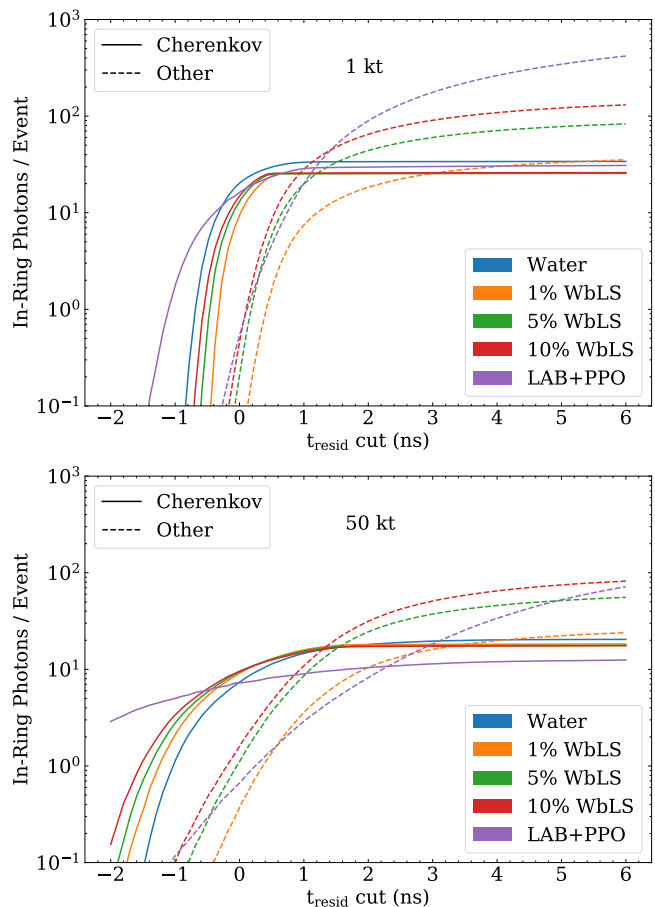


FIG. 4. The number of “in-ring” (see text) photons per event determined using truth information from 2.6 MeV electrons simulated at the center of two detector geometries (top) 1 kt and (bottom) 50 kt. The number of photons is shown as a function of a cut on the t_{resid} distribution, selecting for prompt photons. Cherenkov photons are shown in solid lines, with all other photons shown with dashed lines. The colored legend applies to both Cherenkov and other photons.

in the 1-kt detector, and by less than 50% in the 50-kt detector for 10% WbLS. For LAB+PPO, dispersion (especially in the 50-kt detector) and the relatively slower time profile results in enhanced t_{resid} separation between Cherenkov and scintillation photons, enabling comparable or better angular resolution than the WbLS materials. Notably, the LAPPD model has sufficient time resolution to easily identify a pure population of prompt Cherenkov photons in LAB+PPO resulting from dispersion, allowing direction reconstruction comparable to water. This is not seen with the PMT model, which lacks the time resolution to resolve this population. This indicates that the dispersion of a pure scintillator is a beneficial quality for direction reconstruction, and that the faster timing profiles of the WbLS materials relative to LAB+PPO may be a hindrance to accurate direction reconstruction. The former point may be difficult to address in WbLS, given that the refractive index is very close to that of water

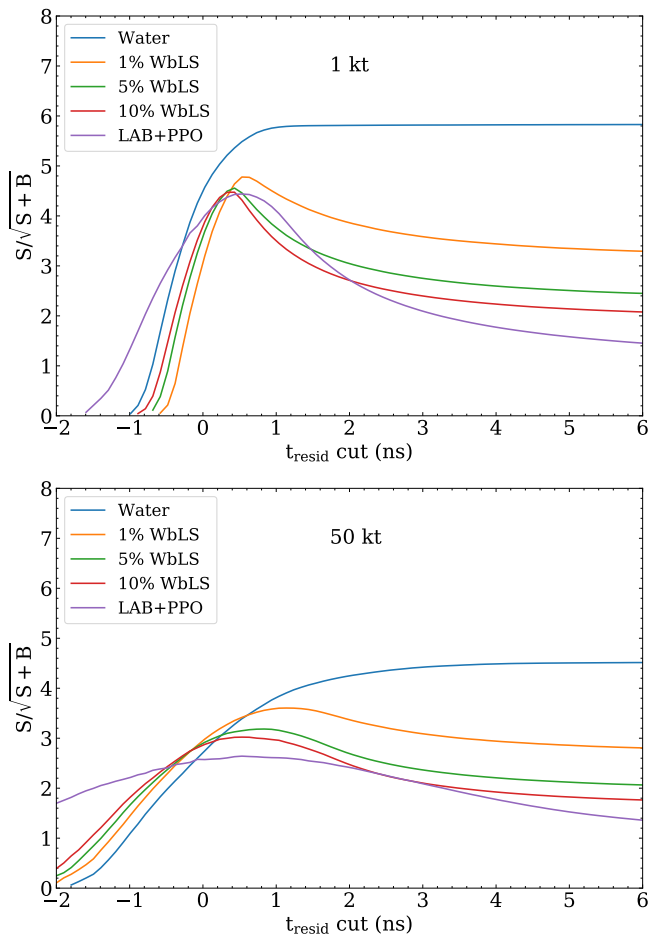


FIG. 5. With S defined as Cherenkov photons and B defined as other photons, these figures plot $S/\sqrt{S+B}$, or the significance of the population of “in-ring” Cherenkov photons, for the data shown in Fig. 4, with the two detector geometries (top) 1 kt and (bottom) 50 kt.

and it is hardly tunable without significantly altering the material. However, the time profiles of liquid scintillators can be adjusted [4, 5], and this is explored in the following section.

V. IMPACT OF SCINTILLATION TIME PROFILE IN A LARGE-SCALE NEUTRINO DETECTOR

Two properties are explored here: the rise time of the profile, τ_r , and a single decay constant, τ_1 , using the form:

$$p(t) = \frac{1}{N}(1 - e^{-t/\tau_r})e^{-t/\tau_1}, \quad (7)$$

where N is a normalization constant. Both the LAB+PPO and 10% WbLS materials have their time profiles adjusted, and reconstruction metrics are shown using the methodology described in Sec. III. We consider

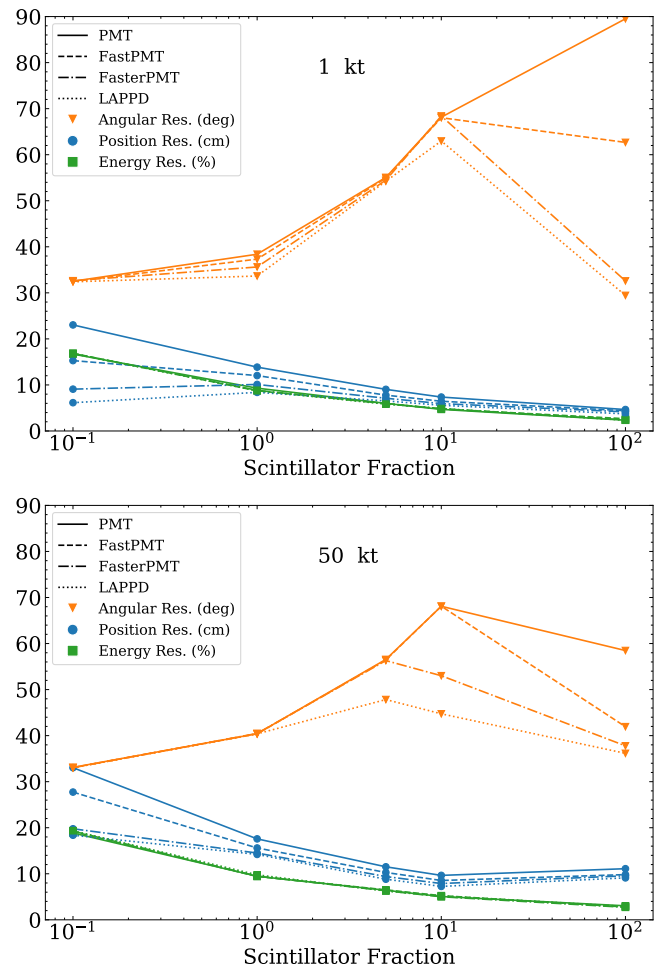


FIG. 6. Reconstruction resolutions of 2.6 MeV electrons simulated at the center of two detector geometries (top) 1-kt and (bottom) 50-kt, differing in size, and four photon detector models (“PMT,” “FastPMT,” “FasterPMT,” and “LAPPD”), differing in TTS. These resolutions are shown as a function of scintillator fraction. Water is artificially plotted at 10^{-1} (due to log scale). Angular resolution is shown for the best prompt cut. See legend for units.

both a scan of the decay constant for two chosen rise times, and a scan of the rise time for two chosen decay times. In all cases, all other properties of the materials (light yield, refractive index, absorption and scattering, emission) are kept constant at the values presented in Sec. II. This allows us to decouple the effect of the time profile from other properties of the scintillator, which may be useful input for guiding future material development.

A. Decay time

The decay constant is scanned from 2.5 ns (typical of current WbLS) to 10 ns (typical of slow scintillators [4, 5]), and the simulation and reconstruction meth-

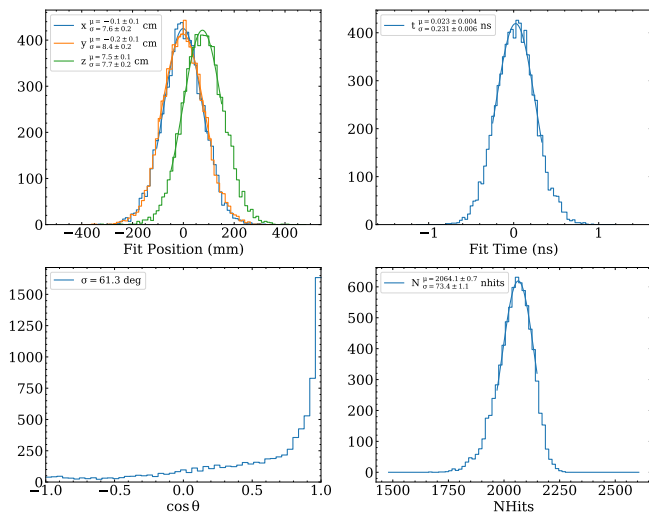


FIG. 7. The upper left panel shows the position fit residuals in three dimensions, where Z is always aligned with the initial event direction. The top right panel shows the fitted time residuals. The $\cos\theta$ fitted event direction distribution is in the bottom left, with the bottom right being the total number of detected photons, from which the energy resolution is calculated. This is shown for the LAB+PPO material in the 1 kt detector geometry using the “PMT” photon detector model and a $t_{resid} < 1.0$ ns prompt cut for direction reconstruction.

ods described in Sec. III are used for each combination. This scan is repeated for two choices of rise time: a fast rise time of 100 ps is used, characteristic of the WbLS cocktails explored in this paper, and a slow rise time of 1 ns, more representative of LAB+PPO.

As before, this is done for 2.6-MeV electrons with both the 1-kt and 50-kt detector geometries. Only the LAPPD photon detector model is explored here, to simplify the presentation of results. Resolution metrics are presented for position and direction with the 10% WbLS and LAB+PPO materials in Fig. 8. Energy resolution is unaffected by changes to the time profile.

Slower decay constants in 10% WbLS appear to improve angular resolution quite significantly in the 1-kt geometry, more so for the faster rise time, but degrade the resolution in the 50-kt geometry. This is likely due to a difference in the impact of dispersion at the different scales (see Fig. 2). If dispersion has already separated the Cherenkov and scintillation photons sufficiently in time, there is no further advantage to slowing the scintillator. Since, in this limit, slowing the decay constants reduces position and time resolution without better separating the Cherenkov population, the angular resolution is degraded.

Notably for LAB+PPO the effects are small, and scanning the decay time has little effect on the angular resolution, and only a small impact on vertex reconstruction over this range. This suggests that the time profile of LAB+PPO may be close to optimal for these purposes.

Simulated hit time residuals in Fig. 2 show that the unmodified LAB+PPO material has a clear prompt Cherenkov population in the 50-kt detector (c.f. 10% WbLS), which is primarily due to dispersion, and is the dominant factor in the good performance of LAB+PPO.

B. Rise time

The rise time is scanned for values from 100 ps to 1 ns, for both a 2.5 ns and 5 ns decay time, characteristic of WbLS and LAB+PPO, respectively. As before, this is done for 2.6-MeV electrons with both the 1-kt and 50-kt detector geometries. Results are shown in Fig. 9.

In all cases, slowing the rise time improves the angular resolution, but slightly degrades the position and time resolution. Slower rise times in 10% WbLS degrade the position and time resolution more than in the LAB+PPO material. 10% WbLS demonstrates significant gains in angular resolution for slower time constants, though for the same position or time resolution, LAB+PPO results in better angular resolution.

VI. IMPACT FOR PHYSICS REACH

We now briefly examine how the energy and angular resolutions evaluated in the previous sections affect the capability for rejection of the ^8B solar neutrino background in NLDBD searches, and identification of signal events for CNO solar neutrino detection. In both cases, identification (as either signal or background) of the directional solar neutrino events is the capability under study.

In order to do so, we again make use of the RAT-PAC framework [56], including the neutrino-electron elastic scattering generator and the radioactive decay generator used by SNO [63] and SNO+ [65] as well as an implementation of Decay0 [66]. In simulation, the neutrino-electron elastic scattering differential cross section [67] is weighted by the neutrino energy spectrum [68] for the different fluxes from the Sun and then sampled in outgoing electron energy and scattering angle, for both ν_e and ν_μ . Solar neutrino fluxes are taken from [69]. The decay energy spectra are also found for various backgrounds associated with the CNO energy region of interest. The solar neutrino interactions and decays are then simulated accordingly to extract the expected energy deposition in the target materials under consideration. After the simulation, solar neutrino event samples are weighted following the survival probability calculated from the B16 GS98 Standard Solar Model [70].

The extracted angular resolution parameters from Secs. IV and V are used to smear the scattering angle for solar neutrino events using a functional form taken from [44], while radioactive and cosmogenic background events, as well as double beta decay events, are assumed to be isotropic.

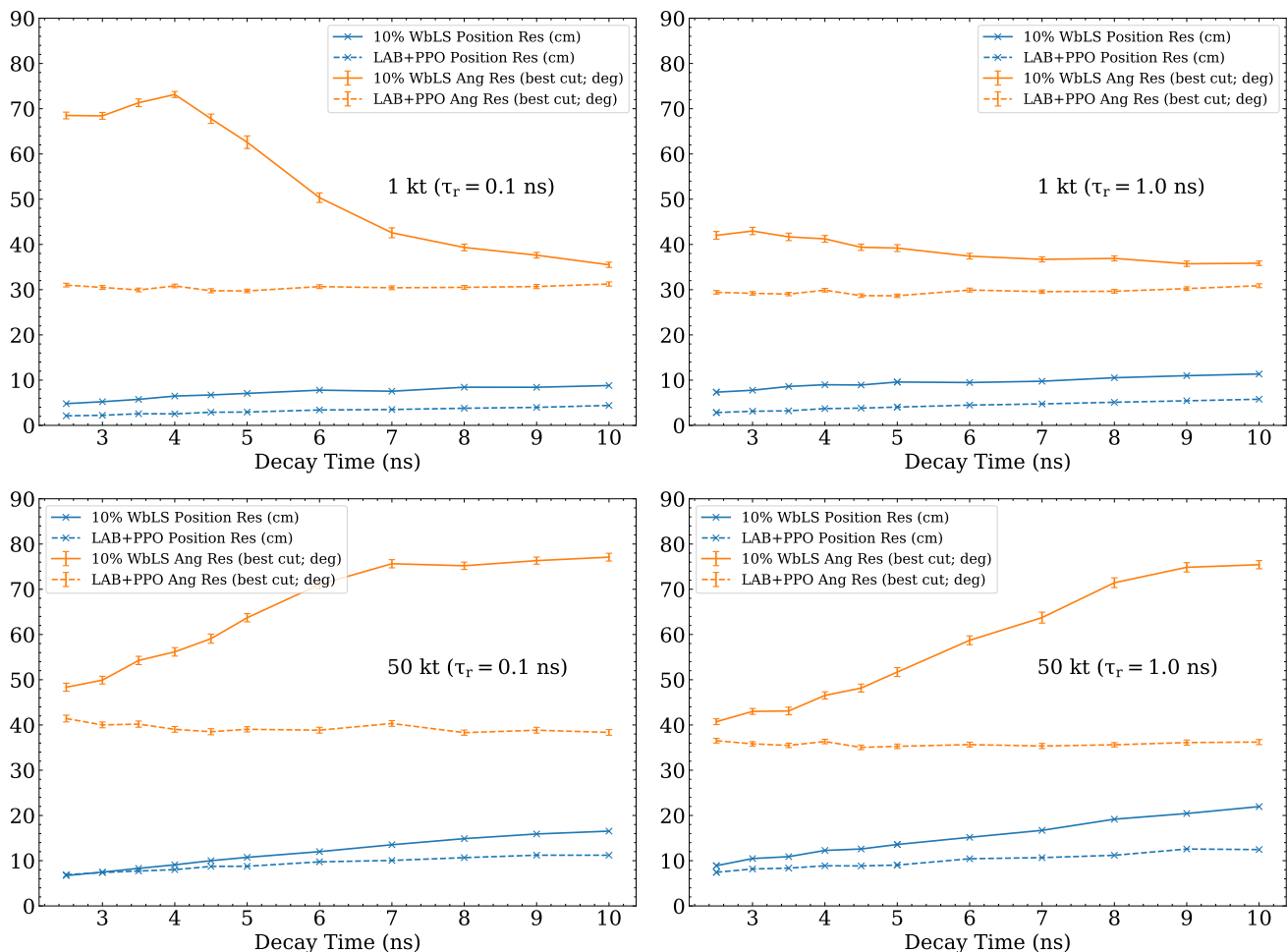


FIG. 8. Reconstruction resolutions for a scan of the scintillation decay time with a rise time of (left) 100 ps and (right) 1 ns in the (top) 1-kt detector geometry and (bottom) 50-kt detector geometry. Results are shown for the LAPPD photon detector model for the 10% WbLS and LAB+PPO materials. Angular resolution is shown for the best prompt cut. See legend for units.

A. NLDBD sensitivity

For the NLDBD study, we consider LAB+PPO loaded with 5% natural Te (34.1% ^{130}Te), and assume the expected $3\%/\sqrt{E}$ energy resolution from [42], since the isotope-loaded scintillator will behave differently from those studied here. We make the same assumptions about location and background rates as in the previous study. The purpose of this study is to explore the impact of the angular resolutions determined in Sec. IV. No assumption on angular resolution was directly made in [42], so we use the angular resolution found here for unloaded scintillator to extend the previous analysis, as being representative of reasonably achievable time profiles. Energy cuts are applied to restrict the study to the $0\nu\beta\beta$ region of interest for ^{130}Te , as outlined in [42]. We further apply cuts as a function of reconstructed direction relative to the Sun, $\cos\theta_{\odot}$, in order to reduce the background from directional ^8B solar neutrinos. The fraction of ν_e and ν_{μ} samples for ^8B neutrinos surviving

these analysis cuts are scaled according to expected event rates on LAB+PPO in order to maintain the correct ratio of ν_e and ν_{μ} interactions and properly calculate the overall efficiency for rejecting solar neutrino background events and accepting isotropic events such as radioactive decays or $0\nu\beta\beta$.

The efficiencies for the cut values are then propagated through the box analysis procedure of [42] to select an optimal cut that yields the best sensitivity. To quote an example, we find an expected sensitivity of $T_{1/2}^{0\nu\beta\beta} > 1.4 \times 10^{28}$ years at 90% CL in the 50-kt, LAPPD-instrumented pure LAB+PPO detector with decay time of 2.5 ns and rise time of 1.0 ns, after 10 years of data taking. This equates to a mass limit of $m_{\beta\beta} < 4.5 - 11.1$ meV, using nuclear matrix elements from [71, 72]. Such a detector achieves an angular resolution of roughly 37° . This result is achieved by cutting on a solar angle corresponding to $\cos\theta_{\odot} = 0.5$, which rejects over 60% of the ^8B background while keeping 75% of the signal. This increases confidence in assumptions of

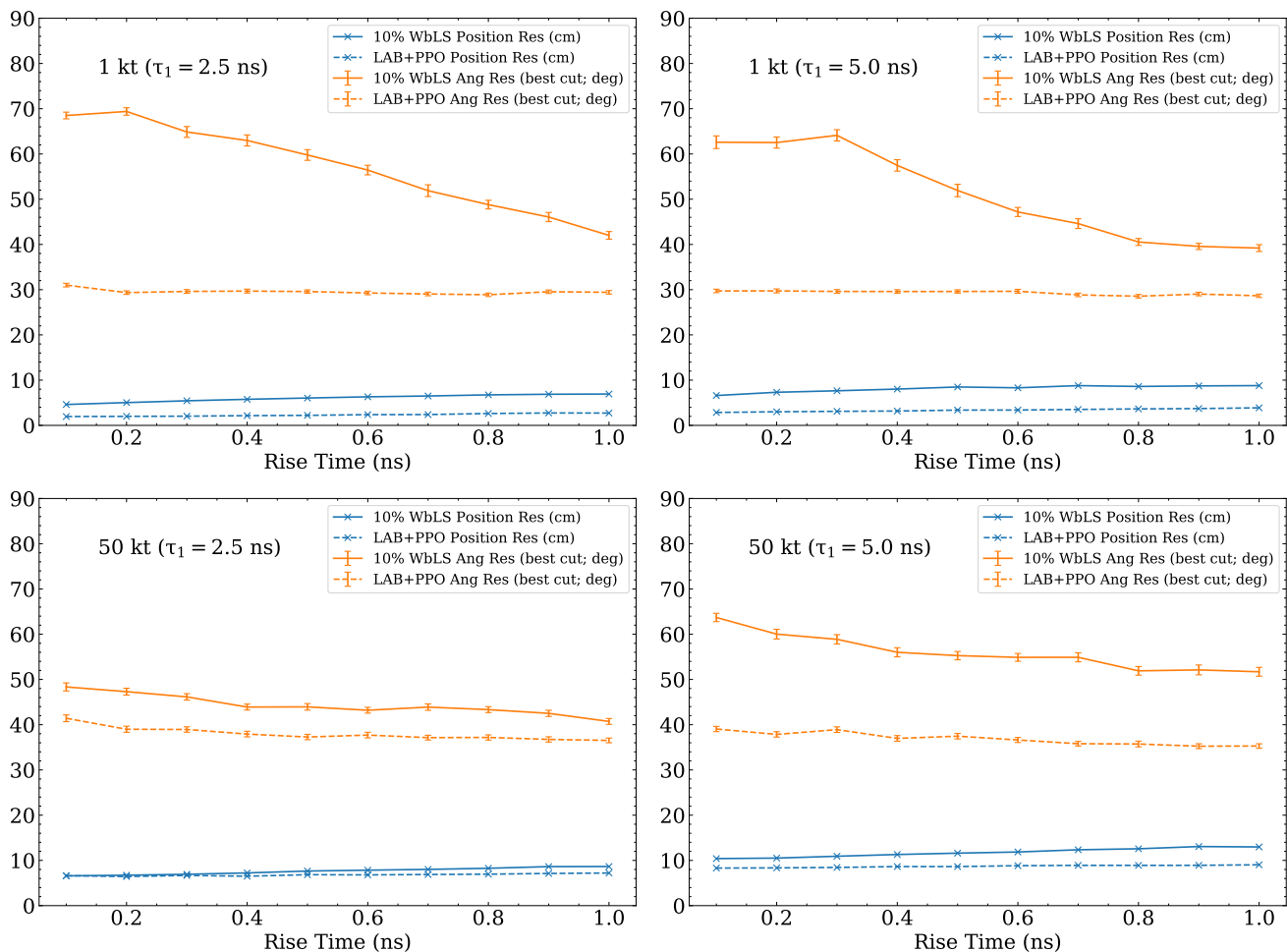


FIG. 9. Reconstruction resolutions when the scintillation rise time is scanned for a decay time of (left) 2.5 ns and (right) 5.0 ns in the (top) 1-kt detector geometry and (bottom) 50-kt detector geometry. This is done using the LAPPD photon detector for the 10% WbLS and LAB+PPO materials. Angular resolution is shown for the best prompt cut. See legend for units.

rejection capability used in [42]. Notably, improving the angular resolution to 30° and performing the same analysis does not yield changes to sensitivity to the leading decimal.

Several other configurations for the 50-kt, LAPPD detector give results with similar sensitivity, to this precision. We see that the impact of scanning the decay time for values from 2.5 to 10 ns for LAB+PPO changes the sensitivity by less than 0.02×10^{28} years, and the sensitivity improves for slower rise times, but the impact of the change from a rise time of 100 ps to 1 ns is less than 0.04×10^{28} years. As such variation of the decay and rise time of the scintillation time profile at the scale examined are not thought to have a large impact on sensitivity to NLDBD. It should be noted that this conclusion is specific to our particular choice of direction reconstruction methodology, and conclusions may differ for other approaches.

B. Precision CNO measurement

We also evaluate scenarios for CNO solar neutrino detection in a manner akin to the large-scale WbLS detector studies presented in [44] and [42]. We make the same assumptions about location and background rates as in those studies. Instead of the hit-based lookup reconstruction scheme applied in those studies, we employ a Gaussian smearing based on the expected number of hits, as determined in Sec. IV. Since quenching effects are fully simulated, we take only the part of the width that is due to photon counting, so as not to double count that effect. The resolution is scaled with energy according to photon statistics. The rest of the fitting procedure remains the same as that described in the mentioned analyses, though we consider the use of a constraint on the *pep* flux at 1.4% from the global analysis of [73], which leverages the information afforded by the full *pp*-chain and solar luminosity on experimental data. This constraint is considered in [74, 75].

We find the expected energy spectra in different LS and WbLS detector configurations according to the energy resolution parameters extracted, using photon statistics only, so as not to double count the uncertainty due to quenching, which is fully simulated. Since the angular resolution evaluated at 2.6 MeV is expected to be much finer than at energies more relevant to the CNO search, for this study, we instead use resolution values determined using simulated electrons at 1.0 MeV. At this energy, we find that in the 50 kt, LAPPD-instrumented detector, the angular resolution achieved by the fitter is 70° for 1% WbLS and 65° for LAB+PPO, as opposed to 40° and 36° respectively at 2.6 MeV. The energy resolution is assumed to vary $\propto 1/\sqrt{E}$ and the angular resolution is assumed to be flat. This does not fully incorporate expected improvements in resolution at higher energies, and degradation at lower energies. A more sophisticated study implementing the full energy dependence is underway. This result is intended to guide the reader as to the capabilities of this style of detector. Energy cuts are applied to the CNO solar neutrino fit region, following the approach in [42]. We consider a threshold of 0.6 MeV in all cases.

We find that in 5 years of data taking, the CNO flux could be determined to a relative uncertainty of 18% (8%) in the 50-kt, LAPPD-instrumented 10% WbLS detector when the *pep* flux is unconstrained (constrained to 1.4%), and to 1% in the same detector filled with LAB+PPO, with the *pep* flux either constrained or unconstrained. We note that the result for the *pep*-constrained case is not very sensitive to the fraction of scintillator in WbLS (1–10% perform similarly) whereas in the *pep*-unconstrained case the performance degrades with reduced scintillator fraction. This is understood because the angular resolution is found to be similar for different WbLS materials at 1 MeV (approximately 70°), so the light yield becomes the critical component in determining performance. A more comprehensive study of these effects will be forthcoming in a future publication.

VII. CONCLUSIONS

In this paper we have considered the low-energy performance of detectors ranging from 1- to 50-kt in size, with a range of target materials. We focus on new measurements of WbLS, and their impacts on detector performance, but consider both pure water and pure scintillator (LAB+PPO) detectors for comparison. We also consider the impact of slowing the scintillation light in both the pure LS and the WbLS. We consider four models for photon detectors, with time resolution of 1.6 ns, 1 ns, 500 ps, and 70 ps. We study detector performance in terms of energy, vertex, and angular resolution, and go on to interpret the results in terms of sensitivity to the CNO solar neutrino flux, and a search for NLDBD.

Performance is determined by the number of detected photons, and their distribution in both time and space.

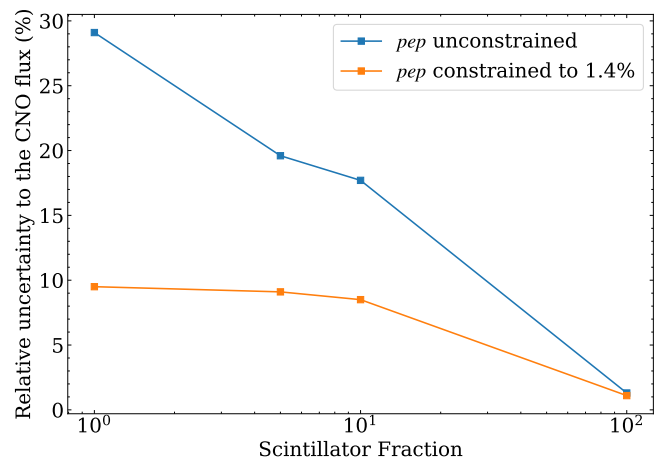


FIG. 10. Precision achieved for a measurement of the CNO flux in a 50-kt detector, as a function of the percentage of LS in the target material, where a value of 10^2 refers to LAB/PPO. Detector performance is based on that found in Sec. IV, assuming the as-measured properties of WbLS and LAB/PPO, without considering possible delays to the scintillation profile. These results use the LAPPD photon detector model.

This depends on both the generated photon distributions, and on effects due to optical propagation. Due to the higher refractive index, more Cherenkov photons are generated in pure scintillator than in water or WbLS, which competes with increased absorption and scattering in this material. Effects of absorption and reemission can be seen in the large detector, where more reemitted photons are detected than direct scintillation photons.

We evaluate energy resolution using the width of the detected hit distribution. As expected, this increases with fraction of scintillator in the target, with minimal impact from the photon detector model.

We employ a likelihood-based evaluation of vertex and direction reconstruction. The scintillation component of WbLS improves the vertex resolution but degrades the angular resolution relative to pure water. The faster time profile of WbLS compared to LAB+PPO makes the identification of the Cherenkov population more challenging, thus hindering direction reconstruction. Dispersion effects play a significant role in the ability to separate Cherenkov photons, particularly in the larger detector. We see that the impact of faster timing photon detectors on low-energy reconstruction performance is important in the larger detector size in order to fully leverage this effect for reconstruction. The higher refractive index of LAB+PPO increases the effects of dispersion for this material. The optimal low-energy angular resolution in a scintillating detector is achieved for LAB+PPO, under the assumption of 70-ps time resolution. For time resolutions of 1 ns or worse, water and WbLS perform better. The difference in performance between WbLS and LAB+PPO is much less significant in the larger detector, where 5% and 10% WbLS perform similarly to

LAB+PPO. Differences are largely due to the fast time profile of WbLS and lower refractive index. It is worth noting that studies of direction reconstruction at high energies may yield different conclusions, given much higher photon statistics.

The fast time profile of WbLS motivated consideration of delaying the time profile, to understand the impact on detector performance. Slow scintillators are under active development, in part for their potential to offer improved angular resolution for low-energy events. This possibility was studied for both 10% WbLS and for LAB+PPO. We observe minimal impact on either position or direction reconstruction for LAB+PPO, but the angular resolution of WbLS can be significantly improved by slowing the scintillation light, to that equivalent to LAB+PPO or even slower, with relatively small impact on vertex resolution.

We consider the impact of the 50-kt detector performance on both CNO solar neutrino detection, and potential for deployment of a containment vessel of Te-loaded LAB+PPO in a larger WbLS detector, for a search for Majorana neutrinos via NLDBD. We find sensitivity to the CNO neutrino flux of better than 20% under conservative assumptions with no constraint on the pep flux, better than 10% in a lightly loaded WbLS detector when considering a constraint on the pep flux, and 1% for a pure LAB+PPO detector, instrumented with fast photon detectors. We find a half life sensitivity of $T_{1/2}^{0\nu\beta\beta} > 1.4 \times 10^{28}$ years at 90% CL for 10 years of data taking, which equates to a mass limit of $m_{\beta\beta} < 4.5 - 11.1$ meV.

There are many correlated factors at work in under-

standing final detector performance. This study relies on a number of measured parameters, but also depends on phenomenological calculations where data does not yet exist, for example for the attenuation and scattering of WbLS. We also emphasize that such a detector could have a high-energy program as well, depending on location, the performance of which has not been studied here and might well produce different conclusions based on different requirements. Further studies and measurements are ongoing, and the results will be updated when those numbers are available.

ACKNOWLEDGMENTS

The authors would like to thank Minfang Yeh, Tanner Kaptanoglu, Michael Wurm, Josh Klein, Bob Svoboda, Matthew Malek and Adam Bernstein for useful discussions. The authors would like to thank the SNO+ collaboration for providing a number of simulation modules, as well as data on the optical properties of LAB/PPO, including the light yield, absorption and reemission spectra, and refractive index.

This material is based upon work supported by the Director, Office of Science, of the U.S. Department of Energy under Contract No. DE-AC02-05CH11231 The project was funded by the U.S. Department of Energy, National Nuclear Security Administration, Office of Defense Nuclear Nonproliferation Research and Development (DNN R&D). This material is based upon work supported by the U.S. Department of Energy, Office of Science, Office of High Energy Physics, under Award Number DE-SC0018974

-
- [1] M. Yeh, S. Hans, W. Beriguete, R. Rosero, L. Hu, R. L. Hahn, M. V. Diwan, D. E. Jaffe, S. H. Kettell, and L. Littenberg, *Nucl. Instrum. Meth. A* **660**, 51 (2011).
- [2] L. Bignell, D. Beznosko, M. Diwan, S. Hans, D. Jaffe, S. Kettell, R. Rosero, H. Themann, B. Viren, E. Worcester, M. Yeh, and C. Zhang, *J. Instrum.* **10**, P12009 (2015).
- [3] C. Buck and M. Yeh, *J. Phys. G* **43**, 093001 (2016).
- [4] Z. Guo, M. Yeh, R. Zhang, D.-W. Cao, M. Qi, Z. Wang, and S. Chen, *Astroparticle Physics* **109**, 33 (2019).
- [5] S. D. Biller, E. J. Leming, and J. L. Paton, *Nucl. Instrum. Meth. A* **972**, 164106 (2020).
- [6] E. Graham, D. Gooding, J. Gruszko, C. Grant, B. Naranjo, and L. Winslow, *J. Instrum.* **14**, P11024 (2019).
- [7] C. Aberle, J. J. Li, S. Weiss, and L. Winslow, *J. Instrum.* **8**, P10015 (2013).
- [8] T. Marrodn Undagoitia, F. von Feilitzsch, L. Oberauer, W. Potzel, A. Ulrich, J. Winter, and M. Wurm, *Review of Scientific Instruments* **80**, 043301 (2009).
- [9] J. Ashenfelter *et al.*, *J. Instrum.* **14**, P03026 (2019).
- [10] J. Cumming, S. Hans, and M. Yeh, *Nucl. Instrum. Meth. A* **925**, 1 (2019).
- [11] A. Abusleme *et al.* (Daya Bay and JUNO), “Optimization of the juno liquid scintillator composition using a daya bay antineutrino detector,” (2020), [arXiv:2007.00314](https://arxiv.org/abs/2007.00314) [physics.ins-det].
- [12] X. Zhou, Q. Liu, M. Wurm, Q. Zhang, Y. Ding, Z. Zhang, Y. Zheng, L. Zhou, J. Cao, and Y. Wang, *Review of Scientific Instruments* **86**, 073310 (2015).
- [13] J. Caravaca, F. B. Descamps, B. J. Land, M. Yeh, and G. D. Orebi Gann, *Eur. Phys. J. C* **77**, 811 (2017).
- [14] J. Caravaca, B. Land, M. Yeh, and G. Orebi Gann, “Characterization of water-based liquid scintillator for Cherenkov and scintillation separation,” (2020), [arXiv:2006.00173](https://arxiv.org/abs/2006.00173) [physics.ins-det].
- [15] J. Gruszko, B. Naranjo, B. Daniel, A. Elagin, D. Gooding, C. Grant, J. Ouellet, and L. Winslow, *J. Instrum.* **14**, P02005 (2019).
- [16] M. Li, Z. Guo, M. Yeh, Z. Wang, and S. Chen, *Nucl. Instrum. Meth. A* **830**, 303 (2016).
- [17] T. Kaptanoglu, M. Luo, and J. Klein, *J. Instrum.* **14**, T05001 (2019).
- [18] T. Kaptanoglu, M. Luo, B. Land, A. Bacon, and J. R. Klein, *Phys. Rev. D* **101**, 072002 (2020).
- [19] A. Lyashenko *et al.*, *Nucl. Instrum. Meth. A* **958**, 162834

- (2020).
- [20] B. W. Adams, A. Elagin, H. J. Frisch, R. Obaid, E. Oberla, A. Vostrikov, R. G. Wagner, J. Wang, and M. Wetstein, *Nucl. Instrum. Meth. A* **795**, 1 (2015).
- [21] E. Ramberg (PSEC), in *Technology and instrumentation in particle physics. Proceedings, 1st International Conference, TIPP09, Tsukuba, Japan, March 12-17, 2009*, Vol. 623 (2010) pp. 316–317.
- [22] E. Oberla and H. J. Frisch, *Nucl. Instrum. Meth. A* **814**, 19 (2016).
- [23] O. H. W. Siegmund *et al.*, in *Proceedings, 2011 IEEE Nuclear Science Symposium and Medical Imaging Conference (NSS/MIC 2011)* (2011) pp. 2063–2070.
- [24] N. Barros, T. Kaptanoglu, B. Kimelman, J. Klein, E. Moore, J. Nguyen, K. Stavreva, and R. Svoboda, *Nucl. Instrum. Meth. A* **852**, 15 (2017).
- [25] J. Brack *et al.*, *Nucl. Instrum. Meth. A* **712** (2012), 10.1016/j.nima.2013.02.022.
- [26] J. Dalmasson, G. Gratta, A. Jamil, S. Kravitz, M. Malek, K. Wells, J. Bentley, S. Steven, and J. Su, *Phys. Rev. D* **97**, 052006 (2018).
- [27] B. S. Wonsak *et al.*, *J. Instrum.* **13**, P07005 (2018).
- [28] B. Wonsak *et al.*, in *Solar Neutrinos: Proceedings of the 5th International Solar Neutrino Conference*, edited by M. Meyer and K. Zuber (World Scientific, Singapore, 2019) pp. 445–463.
- [29] J. Dunger and S. D. Biller, *Nucl. Instrum. Meth. A* **943**, 162420 (2019).
- [30] C. Aberle, A. Elagin, H. J. Frisch, M. Wetstein, and L. Winslow, *J. Instrum.* **9**, P06012 (2014).
- [31] A. Elagin, H. Frisch, B. Naranjo, J. Ouellet, L. Winslow, and T. Wongjirad, *Nucl. Instrum. Meth. A* **849**, 102 (2017).
- [32] R. Jiang and A. Elagin, “Space-Time Discriminant to Separate Double-Beta Decay from ^8B Solar Neutrinos in Liquid Scintillator,” (2019), [arXiv:1902.06912](https://arxiv.org/abs/1902.06912) [physics.ins-det].
- [33] A. Li, A. Elagin, S. Fraker, C. Grant, and L. Winslow, *Nucl. Instrum. Meth. A* **947**, 162604 (2019).
- [34] A. R. Back *et al.* (ANNIE), “Accelerator Neutrino Neutron Interaction Experiment (ANNIE): Preliminary results and physics phase proposal,” (2017), [arXiv:1707.08222v2](https://arxiv.org/abs/1707.08222v2) [physics.ins-det].
- [35] I. Anghel *et al.* (ANNIE), “Expression of Interest: The Atmospheric Neutrino Neutron Interaction Experiment (ANNIE),” (2014), [arXiv:1402.6411](https://arxiv.org/abs/1402.6411) [physics.ins-det].
- [36] I. Anghel *et al.*, “Letter of intent: The Accelerator Neutrino Neutron Interaction Experiment (ANNIE),” (2015), [arXiv:1504.01480](https://arxiv.org/abs/1504.01480) [physics.ins-det].
- [37] A. Bernstein, *AIT-WATCHMAN Conceptual Design Review Report*, Tech. Rep. (Lawrence Livermore National Lab.(LLNL), Livermore, CA (United States), 2019).
- [38] M. Askins *et al.* (WATCHMAN), “The Physics and Nuclear Nonproliferation Goals of WATCHMAN: A Water Cherenkov Monitor for Antineutrinos,” (2015), [arXiv:1502.01132](https://arxiv.org/abs/1502.01132) [physics.ins-det].
- [39] D. L. Danielson *et al.*, “Directionally accelerated detection of an unknown second reactor with antineutrinos for mid-field nonproliferation monitoring,” (2019), [arXiv:1909.05374](https://arxiv.org/abs/1909.05374) [physics.ins-det].
- [40] S.-H. Seo, “Neutrino Telescope at Yemilab, Korea,” (2019), [arXiv:1903.05368](https://arxiv.org/abs/1903.05368) [physics.ins-det].
- [41] M. Wurm *et al.*, *Astroparticle Physics* **35**, 685 (2012).
- [42] M. Askins *et al.*, *Eur. Phys. J. C* **80** (2020), 10.1140/epjc/s10052-020-7977-8.
- [43] J. R. Alonso *et al.*, “Advanced Scintillator Detector Concept (ASDC): A Concept Paper on the Physics Potential of Water-Based Liquid Scintillator,” (2014), [arXiv:1409.5864](https://arxiv.org/abs/1409.5864) [physics.ins-det].
- [44] R. Bonventre and G. D. Orebi Gann, *Eur. Phys. J. C* **78**, 435 (2018).
- [45] S. D. Biller, *Phys. Rev. D* **87**, 071301 (2013).
- [46] S. Andringa *et al.* (SNO+), *Adv. High Energy Phys.* **2016**, 6194250 (2016).
- [47] The SNO+ collaboration, Private communication.
- [48] D. R. Onken, F. Moretti, J. Caravaca, M. Yeh, G. D. Orebi Gann, and E. D. Bourret, *Mater. Adv.* **1**, 71 (2020).
- [49] B. W. Adams *et al.* (LAPPD), “A Brief Technical History of the Large-Area Picosecond Photodetector (LAPPD) Collaboration,” (2016), [arXiv:1603.01843](https://arxiv.org/abs/1603.01843) [physics.ins-det].
- [50] M. Agostini *et al.* (Borexino), *Nature* **562**, 505 (2018).
- [51] A. Gando *et al.* (KamLAND-Zen), *Phys. Rev. Lett.* **117**, 082503 (2016).
- [52] S.-F. Ge and W. Rodejohann, *Phys. Rev. D* **92**, 093006 (2015).
- [53] F. An *et al.* (JUNO), *J. Phys. G* **43**, 030401 (2016).
- [54] P. Bakhti and A. Y. Smirnov, *Phys. Rev. D* **101**, 123031 (2020).
- [55] S. Agostinelli *et al.* (GEANT4), *Nucl. Instrum. Meth. A* **506**, 250 (2003).
- [56] “RAT-PAC User’s Guide,” <https://rat.readthedocs.io/en/latest/>.
- [57] J. C. R. Reis *et al.*, *ChemPhysChem* **11**, 3722.
- [58] “International association for the properties of water and steam,” <http://www.iapws.org/>, release of September 1997.
- [59] R. M. Pope and E. S. Fry, *Appl. Opt.* **36**, 8710 (1997).
- [60] R. C. Smith and K. S. Baker, *Appl. Opt.* **20**, 177 (1981).
- [61] J. Caravaca, F. B. Descamps, B. J. Land, J. Wallig, M. Yeh, and G. D. Orebi Gann, *Phys. Rev. C* **95**, 055801 (2017).
- [62] Hamamatsu Photonics K.K., “Photomultiplier tubes and assemblies,” https://www.hamamatsu.com/resources/pdf/etd/High_energy_PMT_TPMZ0003E.pdf (2017).
- [63] B. Aharmim *et al.* (SNO), *Phys. Rev. C* **75**, 045502 (2007).
- [64] P. Virtanen *et al.*, *Nature Methods* **17**, 261 (2020).
- [65] M. Anderson *et al.* (SNO+), *Phys. Rev. D* **99**, 032008 (2019).
- [66] O. Ponkratenko, V. Tretyak, and Y. Zdesenko, *Phys. Atom. Nucl.* **63**, 1282 (2000).
- [67] J. N. Bahcall, M. Kamionkowski, and A. Sirlin, *Phys. Rev. D* **51**, 6146 (1995).
- [68] W. Winter, S. Freedman, K. Rehm, and J. Schiffer, *Phys. Rev. C* **73**, 025503 (2006).
- [69] J. N. Bahcall, A. M. Serenelli, and S. Basu, *Astrophys. J. Lett.* **621**, L85 (2005).
- [70] N. Vinyoles *et al.*, *Astrophys. J.* **835**, 202 (2017).
- [71] T. R. Rodriguez and G. Martinez-Pinedo, *Phys. Rev. Lett.* **105**, 252503 (2010).
- [72] J. Barea, J. Kotila, and F. Iachello, *Phys. Rev. C* **87**, 014315 (2013).
- [73] J. Bergstrom, M. Gonzalez-Garcia, M. Maltoni, C. Pena-Garay, A. M. Serenelli, and N. Song, *J. High Energy Phys.* **03**, 132 (2016).
- [74] M. Agostini *et al.* (Borexino), “Sensitivity to neutri-

nos from the solar CNO cycle in Borexino,” (2020), [arXiv:2005.12829 \[hep-ex\]](#).
[75] M. Agostini *et al.* (Borexino), “First Direct Experimental

Evidence of CNO neutrinos,” (2020), [arXiv:2006.15115 \[hep-ex\]](#).